Biomedical Optics EXPRESS

Quantifying the vascular response to ischemia with speckle variance optical coherence tomography

Kristin M. Poole, Devin R. McCormack, Chetan A. Patil, Craig L. Duvall, and Melissa C. Skala[*]

Department of Biomedical Engineering, Vanderbilt University, VU Station B #351631, Nashville, TN 37235, USA

[*] m.skala@vanderbilt.edu

Abstract: Longitudinal monitoring techniques for preclinical models of vascular remodeling are critical to the development of new therapies for pathological conditions such as ischemia and cancer. In models of skeletal muscle ischemia in particular, there is a lack of quantitative, non-invasive and long term assessment of vessel morphology. Here, we have applied speckle variance optical coherence tomography (OCT) methods to quantitatively assess vascular remodeling and growth in a mouse model of peripheral arterial disease. This approach was validated on two different mouse strains known to have disparate rates and abilities of recovering following induction of hind limb ischemia. These results establish the potential for speckle variance OCT as a tool for quantitative, preclinical screening of pro- and anti-angiogenic therapies.

OCIS codes: (170.4500) Optical coherence tomography; (170.3880) Medical and biological imaging; (170.2655) Functional monitoring and imaging; (100.2960) Image analysis; (110.6150) Speckle imaging.

References and links

1. P. Carmeliet and R. K. Jain, “Angiogenesis in cancer and other diseases,” Nature **407**(6801), 249–257 (2000).
2. D. Hanahan and R. A. Weinberg, “The hallmarks of cancer,” Cell **100**(1), 57–70 (2000).
3. I. Kumar, C. A. Staton, S. S. Cross, M. W. Reed, and N. J. Brown, “Angiogenesis, vascular endothelial growth factor and its receptors in human surgical wounds,” Br. J. Surg. **96**(12), 1484–1491 (2009).
4. G. H. Gibbons and V. J. Dzau, “The emerging concept of vascular remodeling,” N. Engl. J. Med. **330**(20), 1431–1438 (1994).
5. S. Rey and G. L. Semenza, “Hypoxia-inducible factor-1-dependent mechanisms of vascularization and vascular remodelling,” Cardiovasc. Res. **86**(2), 236–242 (2010).
6. S. M. Weis and D. A. Cheresh, “Tumor angiogenesis: molecular pathways and therapeutic targets,” Nat. Med. **17**(11), 1359–1370 (2011).
7. R. Gupta, J. Tongers, and D. W. Losordo, “Human studies of angiogenic gene therapy,” Circ. Res. **105**(8), 724–736 (2009).
8. M. Prewett, J. Huber, Y. Li, A. Santiago, W. O’Connor, K. King, J. Overholser, A. Hooper, B. Pytowski, L. Witte, P. Bohlen, and D. J. Hicklin, “Antivascular endothelial growth factor receptor (fetal liver kinase 1) monoclonal antibody inhibits tumor angiogenesis and growth of several mouse and human tumors,” Cancer Res. **59**(20), 5209–5218 (1999).
9. K. Lee, D. Z. Qian, S. Rey, H. Wei, J. O. Liu, and G. L. Semenza, “Anthracycline chemotherapy inhibits HIF-1 transcriptional activity and tumor-induced mobilization of circulating angiogenic cells,” Proc. Natl. Acad. Sci. U.S.A. **106**(7), 2353–2358 (2009).
10. A. Rege, N. V. Thakor, K. Rhie, and A. P. Pathak, “In vivo laser speckle imaging reveals microvascular remodeling and hemodynamic changes during wound healing angiogenesis,” Angiogenesis **15**(1), 87–98 (2012).
11. J. Qin, R. Reif, Z. Zhi, S. Dziennis, and R. Wang, “Hemodynamic and morphological vasculature response to a burn monitored using a combined dual-wavelength laser speckle and optical microangiography imaging system,” Biomed. Opt. Express **3**(3), 455–466 (2012).
12. T. Couffinhal, M. Silver, L. P. Zheng, M. Kearney, B. Witzenbichler, and J. M. Isner, “Mouse model of angiogenesis,” Am. J. Pathol. **152**(6), 1667–1679 (1998).

#223146 - $15.00 USD   Received 15 Sep 2014; revised 16 Oct 2014; accepted 29 Oct 2014; published 3 Nov 2014

13. R. Cao, E. Bråkenhielm, R. Pawliuk, D. Wariaro, M. J. Post, E. Wahlberg, P. Leboulch, and Y. Cao, "Angiogenic synergism, vascular stability and improvement of hind-limb ischemia by a combination of PDGF-BB and FGF-2," Nat. Med. **9**(5), 604–613 (2003).
14. A. Limbourg, T. Korff, L. C. Napp, W. Schaper, H. Drexler, and F. P. Limbourg, "Evaluation of postnatal arteriogenesis and angiogenesis in a mouse model of hind-limb ischemia," Nat. Protoc. **4**(12), 1737–1748 (2009).
15. D. Scholz, T. Ziegelhoeffer, A. Helisch, S. Wagner, C. Friedrich, T. Podzuweit, and W. Schaper, "Contribution of arteriogenesis and angiogenesis to postocclusive hindlimb perfusion in mice," J. Mol. Cell. Cardiol. **34**(7), 775–787 (2002).
16. A. Helisch, S. Wagner, N. Khan, M. Drinane, S. Wolfram, M. Heil, T. Ziegelhoeffer, U. Brandt, J. D. Pearlman, H. M. Swartz, and W. Schaper, "Impact of mouse strain differences in innate hindlimb collateral vasculature," Arterioscler. Thromb. Vasc. Biol. **26**(3), 520–526 (2005).
17. C. L. Duvall, W. R. Taylor, D. Weiss, and R. E. Guldberg, "Quantitative microcomputed tomography analysis of collateral vessel development after ischemic injury," Am. J. Physiol. Heart Circ. Physiol. **287**(1), H302–H310 (2004).
18. C. L. Duvall, D. Weiss, S. T. Robinson, F. M. Alameddine, R. E. Guldberg, and W. R. Taylor, "The role of osteopontin in recovery from hind limb ischemia," Arterioscler. Thromb. Vasc. Biol. **28**(2), 290–295 (2007).
19. G. M. Palmer, A. N. Fontanella, S. Shan, G. Hanna, G. Zhang, C. L. Fraser, and M. W. Dewhirst, "In vivo optical molecular imaging and analysis in mice using dorsal window chamber models applied to hypoxia, vasculature and fluorescent reporters," Nat. Protoc. **6**(9), 1355–1366 (2011).
20. E. B. Brown, R. B. Campbell, Y. Tsuzuki, L. Xu, P. Carmeliet, D. Fukumura, and R. K. Jain, "In vivo measurement of gene expression, angiogenesis and physiological function in tumors using multiphoton laser scanning microscopy," Nat. Med. **7**(7), 864–868 (2001).
21. H. F. Zhang, K. Maslov, G. Stoica, and L. V. Wang, "Functional photoacoustic microscopy for high-resolution and noninvasive in vivo imaging," Nat. Biotechnol. **24**(7), 848–851 (2006).
22. L. V. Wang and L. Gao, "Photoacoustic microscopy and computed tomography: from bench to bedside," Annu. Rev. Biomed. Eng. **16**(1), 155–185 (2014).
23. A. K. Dunn, H. Bolay, M. A. Moskowitz, and D. A. Boas, "Dynamic imaging of cerebral blood flow using laser speckle," J. Cereb. Blood Flow Metab. **21**(3), 195–201 (2001).
24. D. E. Goertz, J. L. Yu, R. S. Kerbel, P. N. Burns, and F. S. Foster, "High-frequency 3-D color-flow imaging of the microcirculation," Ultrasound Med. Biol. **29**(1), 39–51 (2003).
25. C. Jacoby, Y. C. Böring, A. Beck, A. Zernecke, V. Aurich, C. Weber, J. Schrader, and U. Flögel, "Dynamic changes in murine vessel geometry assessed by high-resolution magnetic resonance angiography: a 9.4T study," J. Magn. Reson. Imaging **28**(3), 637–645 (2008).
26. K. M. Poole, J. M. Tucker-Schwartz, W. W. Sit, A. J. Walsh, C. L. Duvall, and M. C. Skala, "Quantitative optical imaging of vascular response in vivo in a model of peripheral arterial disease," Am. J. Physiol. Heart Circ. Physiol. **305**(8), H1168–H1180 (2013).
27. B. J. Vakoc, R. M. Lanning, J. A. Tyrrell, T. P. Padera, L. A. Bartlett, T. Stylianopoulos, L. L. Munn, G. J. Tearney, D. Fukumura, R. K. Jain, and B. E. Bouma, "Three-dimensional microscopy of the tumor microenvironment in vivo using optical frequency domain imaging," Nat. Med. **15**(10), 1219–1223 (2009).
28. J. G. Fujimoto, "Optical coherence tomography for ultrahigh resolution in vivo imaging," Nat. Biotechnol. **21**(11), 1361–1367 (2003).
29. B. J. Vakoc, D. Fukumura, R. K. Jain, and B. E. Bouma, "Cancer imaging by optical coherence tomography: preclinical progress and clinical potential," Nat. Rev. Cancer **12**(5), 363–368 (2012).
30. V. J. Srinivasan, J. Y. Jiang, M. A. Yaseen, H. Radhakrishnan, W. Wu, S. Barry, A. E. Cable, and D. A. Boas, "Rapid volumetric angiography of cortical microvasculature with optical coherence tomography," Opt. Lett. **35**(1), 43–45 (2010).
31. J. A. Izatt, M. D. Kulkarni, S. Yazdanfar, J. K. Barton, and A. J. Welch, "In vivo bidirectional color Doppler flow imaging of picoliter blood volumes using optical coherence tomography," Opt. Lett. **22**(18), 1439–1441 (1997).
32. S. Yazdanfar, M. Kulkarni, and J. Izatt, "High resolution imaging of in vivo cardiac dynamics using color Doppler optical coherence tomography," Opt. Express **1**(13), 424–431 (1997).
33. A. Mariampillai, B. A. Standish, E. H. Moriyama, M. Khurana, N. R. Munce, M. K. Leung, J. Jiang, A. Cable, B. C. Wilson, I. A. Vitkin, and V. X. Yang, "Speckle variance detection of microvasculature using swept-source optical coherence tomography," Opt. Lett. **33**(13), 1530–1532 (2008).
34. H. C. Hendargo, R. Estrada, S. J. Chiu, C. Tomasi, S. Farsiu, and J. A. Izatt, "Automated non-rigid registration and mosaicing for robust imaging of distinct retinal capillary beds using speckle variance optical coherence tomography," Biomed. Opt. Express **4**(6), 803–821 (2013).
35. W. Drexler and J. G. Fujimoto, "State-of-the-art retinal optical coherence tomography," Prog. Retin. Eye Res. **27**(1), 45–88 (2008).
36. D. Y. Kim, J. Fingler, J. S. Werner, D. M. Schwartz, S. E. Fraser, and R. J. Zawadzki, "In vivo volumetric imaging of human retinal circulation with phase-variance optical coherence tomography," Biomed. Opt. Express **2**(6), 1504–1513 (2011).

37. U. Schmidt-Erfurth, R. A. Leitgeb, S. Michels, B. Povazay, S. Sacu, B. Hermann, C. Ahlers, H. Sattmann, C. Scholda, A. F. Fercher, and W. Drexler, “Three-dimensional ultrahigh-resolution optical coherence tomography of macular diseases,” Invest. Ophthalmol. Vis. Sci. **46**(9), 3393–3402 (2005).
38. T. Schmoll, C. Kolbitsch, and R. A. Leitgeb, “Ultra-high-speed volumetric tomography of human retinal blood flow,” Opt. Express **17**(5), 4166–4176 (2009).
39. S. Zotter, M. Pircher, T. Torzicky, B. Baumann, H. Yoshida, F. Hirose, P. Roberts, M. Ritter, C. Schütze, E. Götzinger, W. Trasischker, C. Vass, U. Schmidt-Erfurth, and C. K. Hitzenberger, “Large-field high-speed polarization sensitive spectral domain OCT and its applications in ophthalmology,” Biomed. Opt. Express **3**(11), 2720–2732 (2012).
40. B. Davoudi, M. Morrison, K. Bizheva, V. X. Yang, R. Dinniwell, W. Levin, and I. A. Vitkin, “Optical coherence tomography platform for microvascular imaging and quantification: initial experience in late oral radiation toxicity patients,” J. Biomed. Opt. **18**(7), 076008 (2013).
41. Y. Zhao, Z. Chen, C. Saxer, S. Xiang, J. F. de Boer, and J. S. Nelson, “Phase-resolved optical coherence tomography and optical Doppler tomography for imaging blood flow in human skin with fast scanning speed and high velocity sensitivity,” Opt. Lett. **25**(2), 114–116 (2000).
42. J. Enfield, E. Jonathan, and M. Leahy, “In vivo imaging of the microcirculation of the volar forearm using correlation mapping optical coherence tomography (cmOCT),” Biomed. Opt. Express **2**(5), 1184–1193 (2011).
43. A. Mariampillai, M. K. Leung, M. Jarvi, B. A. Standish, K. Lee, B. C. Wilson, A. Vitkin, and V. X. Yang, “Optimized speckle variance OCT imaging of microvasculature,” Opt. Lett. **35**(8), 1257–1259 (2010).
44. M. C. Skala, A. Fontanella, H. Hendargo, M. W. Dewhirst, and J. A. Izatt, “Combined hyperspectral and spectral domain optical coherence tomography microscope for noninvasive hemodynamic imaging,” Opt. Lett. **34**(3), 289–291 (2009).
45. M. C. Skala, A. Fontanella, L. Lan, J. A. Izatt, and M. W. Dewhirst, “Longitudinal optical imaging of tumor metabolism and hemodynamics,” J. Biomed. Opt. **15**(1), 011112 (2010).
46. B. A. Standish, V. X. D. Yang, N. R. Munce, L. M. Wong Kee Song, G. Gardiner, A. Lin, Y. I. Mao, A. Vitkin, N. E. Marcon, and B. C. Wilson, “Doppler optical coherence tomography monitoring of microvascular tissue response during photodynamic therapy in an animal model of Barrett’s esophagus,” Gastrointest. Endosc. **66**(2), 326–333 (2007).
47. Z. Zhi, W. Cepurna, E. Johnson, T. Shen, J. Morrison, and R. K. Wang, “Volumetric and quantitative imaging of retinal blood flow in rats with optical microangiography,” Biomed. Opt. Express **2**(3), 579–591 (2011).
48. M. W. Jenkins, M. Watanabe, and A. M. Rollins, “Longitudinal Imaging of Heart Development With Optical Coherence Tomography,” IEEE J Sel. Top. Quantum Electron. **18**(3), 1166–1175 (2012).
49. Y. Jia, J. Qin, Z. Zhi, and R. K. Wang, “Ultrahigh sensitive optical microangiography reveals depth-resolved microcirculation and its longitudinal response to prolonged ischemic event within skeletal muscles in mice,” J. Biomed. Opt. **16**(8), 086004 (2011).
50. K. M. Poole, C. A. Patil, C. E. Nelson, D. R. McCormack, M. C. Madonna, C. L. Duvall, and M. C. Skala, “Longitudinal study of arteriogenesis with swept source optical coherence tomography and hyperspectral imaging,” Proc. SPIE **8934**, 89341Z (2014).
51. S. Zbinden, L. C. Clavijo, B. Kantor, H. Morsli, G. A. Cortes, J. A. Andrews, G. J. Jang, M. S. Burnett, and S. E. Epstein, “Interanimal variability in preexisting collaterals is a major factor determining outcome in experimental angiogenesis trials,” Am. J. Physiol. Heart Circ. Physiol. **292**(4), H1891–H1897 (2006).
52. D. Chalothorn and J. E. Faber, “Strain-dependent variation in collateral circulatory function in mouse hindlimb,” Physiol. Genomics **42**(3), 469–479 (2010).
53. J. K. Meisner, B. H. Annex, and R. J. Price, “Despite normal arteriogenic and angiogenic responses, hind limb perfusion recovery and necrotic and fibroadipose tissue clearance are impaired in matrix metalloproteinase 9-deficient mice,” J Vasc Surg (posted 28 February 2014, in press).
54. M. S. Mahmud, D. W. Cadotte, B. Vuong, C. Sun, T. W. Luk, A. Mariampillai, and V. X. Yang, “Review of speckle and phase variance optical coherence tomography to visualize microvascular networks,” J. Biomed. Opt. **18**(5), 050901 (2013).
55. A. F. Frangi, W. J. Niessen, K. L. Vincken, and M. A. Viergever, “Multiscale vessel enhancement filtering,” Lect. Notes Comput. Sci. **1496**, 130–137 (1998).
56. S. Yousefi, J. Qin, Z. Zhi, and R. K. Wang, “Label-free optical lymphangiography: development of an automatic segmentation method applied to optical coherence tomography to visualize lymphatic vessels using Hessian filters,” J. Biomed. Opt. **18**(8), 086004 (2013).
57. D. Kroon, “Hessian based Frangi vesselness filter” (2009), retrieved http://www.mathworks.com/matlabcentral/fileexchange/24409-hessian-based-frangi-vesselness-filter.
58. R. Reif, J. Qin, L. An, Z. Zhi, S. Dziennis, and R. Wang, “Quantifying optical microangiography images obtained from a spectral domain optical coherence tomography system,” Int. J. Biomed. Imaging **2012**, 509783 (2012).
59. M. E. Seaman, S. M. Peirce, and K. Kelly, “Rapid analysis of vessel elements (RAVE): a tool for studying physiologic, pathologic and tumor angiogenesis,” PLoS ONE **6**(6), e20807 (2011).
60. N. Landázuri, G. Joseph, R. E. Guldberg, and W. R. Taylor, “Growth and regression of vasculature in healthy and diabetic mice after hindlimb ischemia,” Am. J. Physiol. Regul. Integr. Comp. Physiol. **303**(1), R48–R56 (2012).

#223146 - $15.00 USD Received 15 Sep 2014; revised 16 Oct 2014; accepted 29 Oct 2014; published 3 Nov 2014

61. L. Conroy, R. S. DaCosta, and I. A. Vitkin, "Quantifying tissue microvasculature with speckle variance optical coherence tomography," Opt. Lett. **37**(15), 3180–3182 (2012).
62. T. Schmoll, A. S. Singh, C. Blatter, S. Schriefl, C. Ahlers, U. Schmidt-Erfurth, and R. A. Leitgeb, "Imaging of the parafoveal capillary network and its integrity analysis using fractal dimension," Biomed. Opt. Express **2**(5), 1159–1168 (2011).
63. A. Unterhuber, B. Povazay, B. Hermann, H. Sattmann, A. Chavez-Pirson, and W. Drexler, "In vivo retinal optical coherence tomography at 1040 nm - enhanced penetration into the choroid," Opt. Express **13**(9), 3252–3258 (2005).
64. R. Reif, U. Baran, and R. K. Wang, "Motion artifact and background noise suppression on optical microangiography frames using a naïve Bayes mask," Appl. Opt. **53**(19), 4164–4171 (2014).
65. G. Liu and R. Wang, "Stripe motion artifact suppression in phase-resolved OCT blood flow images of the human eye based on the frequency rejection filter," Chin. Opt. Lett. **11**(3), 031701 (2013).
66. M. F. Kraus, B. Potsaid, M. A. Mayer, R. Bock, B. Baumann, J. J. Liu, J. Hornegger, and J. G. Fujimoto, "Motion correction in optical coherence tomography volumes on a per A-scan basis using orthogonal scan patterns," Biomed. Opt. Express **3**(6), 1182–1199 (2012).
67. S. Yousefi, Z. Zhi, and R. K. Wang, "Eigendecomposition-based clutter filtering technique for optical micro-angiography," IEEE Trans. Biomed. Eng. **58**(8), 2316–2323 (2011).

1. Introduction

Vascular remodeling plays an important role in a broad range of pathological conditions including cancer [1, 2], wound healing [3], and cardiovascular disorders such as atherosclerosis, ischemia, stroke, and hypertension [1, 4, 5]. In cancer, tumor cells manipulate their microenvironment to drive remodeling and facilitate growth [6]. Wound healing also requires angiogenesis to support transport of nutrients, inflammatory cells, and debris during the tissue repair process [3]. In cardiovascular diseases, vascular remodeling often involves insufficient vascular growth. The status of the local tissue environment, such as inflammation, hypoxia, and hemodynamics can drive these changes [1, 5]. In addition to the importance of understanding these processes at a basic science level, the ability to quantitatively evaluate the therapeutic potential of pro- and anti-angiogenic therapies in preclinical models is necessary to improve success in clinical trials [1, 7]. Characterization of vascular remodeling and screening of novel therapies are often performed in animal models of cancer [1, 8, 9], wounds [10, 11], and cardiovascular disease [5, 7, 12–14]. Vascular remodeling is a dynamic and complex process, so non-invasive tools that can quantify *in vivo* vascular remodeling over time are desirable.

Currently, a combination of post-mortem and *in vivo* methods is generally used to provide insight into vascular remodeling in a wide range of preclinical models. Information on vascular density (vessel number and lumen area) is often obtained from histological evaluation of CD31 and α-smooth muscle actin expression in excised tissue [9, 12–14]. However, this technique cannot provide longitudinal data in individual animals. Similarly, x-ray angiography [13, 15, 16] and microcomputed tomography (micro-CT) [17, 18] provide vessel morphology data, but are terminal endpoints that require contrast agents. Several *in vivo* imaging methods have also been employed to evaluate vascular remodeling over time, including fluorescence microscopy [19, 20], photoacoustic microscopy [21, 22], laser speckle imaging [10, 23], high frequency ultrasound [24], and magnetic resonance (MR) angiography [16, 25]. These methods provide the advantage of assessing dynamic changes in the vasculature within individual animals, but there are often trade-offs between resolution, field of view, and imaging depth. For example, MR angiography and high frequency ultrasound provide relatively low resolution (~100 μm) images of vasculature but can penetrate deeper within tissue [24, 25], while microscopy provides higher resolution (sub-micron) images of vasculature at relatively shallow depths of approximately 0.2 mm [19]. Photoacoustic microscopy somewhat improves upon the penetration depth of fluorescence microscopy with a depth of ~0.5 mm while maintaining axial resolution on the order of 10 μm [22]. Laser speckle imaging provides vascular maps with approximately 10-25 μm resolution and covers larger spatial areas than microscopy, but data are two dimensional and superficial (< 1 mm) [10, 23]. While each of these methods has been successfully applied to assess vascular

#223146 - $15.00 USD Received 15 Sep 2014; revised 16 Oct 2014; accepted 29 Oct 2014; published 3 Nov 2014

morphology in preclinical studies, there are trade-offs with each and the ideal methodology is application-specific. One widely used model of vascular remodeling and growth is the mouse hind limb ischemia (HLI) model of peripheral arterial disease (PAD), which is often used as a platform for testing novel therapies [12]. However, there is a lack of non-invasive techniques to quantitatively monitor relevant physiological endpoints longitudinally in the same animal. In the case of the mouse HLI model, methods that provide high resolution images of the vasculature (order of microns) over a depth and field of view (several millimeters) suitable for monitoring skeletal muscle are needed.

Optical coherence tomography (OCT) is well-suited to fill this niche for assessing vascular remodeling in the mouse HLI model [26]. In comparison to other imaging techniques, OCT fills a gap in resolution, field of view, and imaging depth [27, 28]. OCT collects three-dimensional data sets rapidly with resolution on the order of microns, imaging depths of ~1-3 mm, and fields of view consisting of several millimeters [28–30]. Furthermore, OCT imaging of the vasculature does not require exogenous contrast agents, since Doppler [31, 32] and speckle variance [33] OCT techniques provide spatially-resolved detection of blood flow. Vascular imaging with OCT has been demonstrated in humans for ophthalmology applications [34–39], oral microvasculature [40], and microcirculation in the skin [41, 42]. OCT has also been applied to image vasculature in numerous preclinical studies, including normal [43] or tumor [27, 44, 45] vasculature in window chamber models, cortical microvasculature [30], photodynamic therapy effects in a Barrett's esophagus model [46], retinal blood flow [47], burn wounds [11], developing vasculature in embryos [48], and ischemia effects in skeletal muscle [26, 49, 50]. Although the utility of OCT for providing high resolution images of microvasculature has been well established and significant advances have been made in image processing and quantification methods, there remains a lack of quantitative metrics for assessment of vascular morphology over extended time courses (days to weeks) that are relevant in the model of hind limb ischemia.

In this work, we have applied swept-source speckle variance OCT for quantitative, longitudinal assessment of vascular formation and remodeling over 3 weeks in the mouse HLI model of PAD. In contrast to vascular imaging studies in which the skin covering tumors is replaced with a window [27, 44, 45] or a skin incision is made to expose skeletal muscle [49], this study implements non-invasive imaging through the skin of the hind limb. As a result, confounding factors that can influence the vascular response to ischemia are minimized, and individual animals can be tracked over time, thus minimizing the effects of inter-animal variability [51]. In prior work, the use of OCT in this model was validated against standard techniques, and qualitative assessment of morphological changes with time was performed using a 20 kHz 860 nm spectral domain OCT system [26]. Here, we have extracted quantitative morphology metrics using a 100 kHz 1060 nm swept-source OCT system capable of imaging over a wider area with improved imaging depth. We tested our metrics using the well-known phenomenon of strain-dependent variation in recovery from hind limb ischemia [15, 16, 52].

2. Methods

2.1 Animal model

Mouse strains with known robust (FVB) and poor (Balb/c) recovery to hind limb ischemia [15, 16, 52, 53] were used in this study to show that quantitative vascular imaging with OCT can resolve known differences in recovery over time. Unilateral hind limb ischemia [12] was surgically induced in male FVB and Balb/c mice (Jackson Laboratories) by ligation of the right femoral artery and vein with 6-0 silk sutures at two locations: immediately proximal to the origins of the superficial epigastric artery and deep branch of the femoral artery, and proximal to the vessels that branch toward the knee (Fig. 1(A)). Side branches between these points were also ligated, and the segment of the femoral artery and vein between the most

#223146 - $15.00 USD Received 15 Sep 2014; revised 16 Oct 2014; accepted 29 Oct 2014; published 3 Nov 2014

proximal and distal ligation points was excised. The skin incision was closed with interrupted 5-0 nylon sutures. Surgery was performed under isoflurane anesthesia with animals maintained at normal body temperature. Analgesia (10 mg/kg ketoprofen) was administered subcutaneously pre-operatively and every 24 hours post-operatively until animals exhibited normal appearance and behavior. Each animal's contralateral limb served as an internal control. Mice were fed a standard chow diet ad libitum and had free access to water. All protocols were approved by the Institutional Animal Care and Use Committee of Vanderbilt University and done in accordance with the National Institutes of Health *Guide for the Care and Use of Laboratory Animals*.

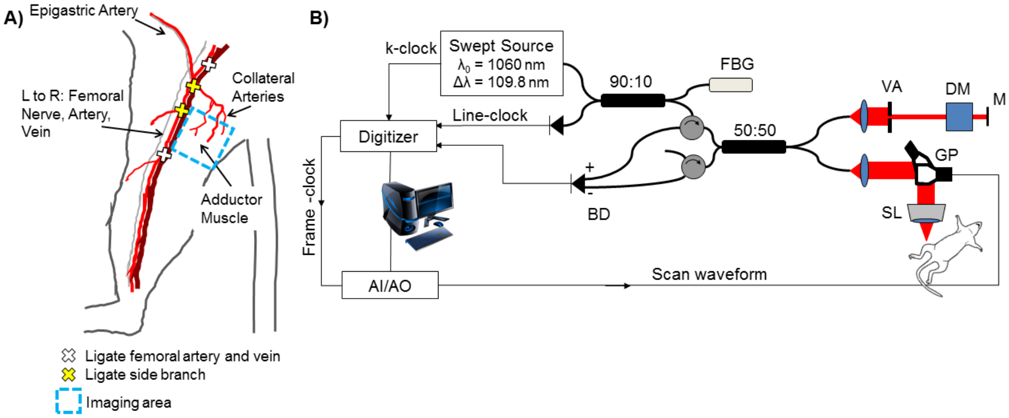

Fig. 1. The hind limb ischemia model is depicted in (A) with vessel ligation points and the imaging area of interest in the adductor muscle region. A schematic of the swept-source OCT system with a 1060 nm center wavelength, 100 kHz sweep-rate source (Axsun) is shown in (B). Lateral and axial resolution are 16 µm and 6.5 µm in air, respectively. FBG – fiber Bragg grating. BD – balanced detector. AI/AO – Analog input/analog output. VA – variable attenuator. DM – dispersion matching cube. M – mirror. SL – scan lens. GP – galvo pair.

2.2 Swept-source optical coherence tomography

The swept-source OCT system (Fig. 1(B)) has a center wavelength of 1060 nm, line rate of 100 kHz (Axsun Technologies, Inc.), lateral / axial resolution of 16 µm / 6.5 µm in air, and 5.7 mW incident at the sample [50]. Speckle variance OCT volumes were collected over a 4 mm x 4 mm area in the adductor muscle region medial to the site of femoral artery excision to monitor remodeling of collateral vessels during recovery from HLI. Mice were imaged under isoflurane anesthesia (1.5%), and secured in a supine position on top of a heating pad to maintain normal body temperature. The imaged area was further stabilized with a coverslip and index matching media. Reference marks were made on the skin of the limb with tissue marking dye to assist in alignment of the OCT system at the same region of interest for each time point. OCT volumes were 1334 A-lines per B-scan, 667 B-scans per C-scan, and 1024 pixels in the depth dimension. The resulting B-scan time was 13.34 ms, with a duty cycle of 80% and B-scan rate of 59.97 Hz. The oversampled A-lines (1334 per B-scan) were averaged over every two lines after computing the magnitude of the complex OCT data, in order to increase the signal-to-noise ratio of the magnitude data and produce higher quality speckle variance maps of the microvasculature. The resulting 6-µm sampling density (667 lines per 4 mm B-scan) exceeds the Nyquist criterion with 2.5 samples within the 16-µm lateral resolution and produces images that maximize the optical performance of the system.

Eight repeated B-scans were collected for each spatial position to allow for speckle variance image processing (Fig. 2), resulting in an acquisition time of 133.4 ms for each speckle variance frame and a total of 88.98 s for each volume. To visualize vascular morphology from the OCT volumes, the variance in structural images was computed over the repeated B-scans [33]. In order to best visualize the slowest flowing vessels, we selected the longest speckle observation time over which decorrelation due to bulk tissue motion did not degrade contrast in the speckle variance projections [43]. In our system, this resulted in a gate length of eight frames. The tissue was segmented in each structural (OCT magnitude) image by applying edge-detection to determine the tissue surface and an intensity threshold to exclude noise due to signal fall-off in depth. The segmented tissue mask was first applied to the speckle variance maps, which were then median filtered and de-shadowed using a step-down exponential filter [54]. Next, bulk motion artifacts were minimized by plotting the average speckle variance for each B-scan in the volume (Fig. 2), and identifying B-scans with high average variance which corresponded with bulk motion artifacts. The speckle variance B-scans with motion artifacts were then replaced with the average of the nearest bulk motion-free speckle variance B-scans, and an average intensity projection over ~1.5 mm in the depth dimension (starting from the tissue surface in each axial scan) was computed to visualize all vessels within the volume in a 2D image. A Hessian filtering algorithm was then used to enhance contrast and connectivity in the depth-projected images of the vasculature [55–57]. In this step, vessels are detected using the eigenvalues of the image [56], and detection is sensitive to vessels in any orientation. Vessel detection was performed over multiple vessel scales (from ~6 to 270 µm in diameter), and the maximum filter response for each pixel was used to scale the input projection image. The resulting scaled image was thresholded to produce a binary mask of the vasculature. Quantitative vascular morphology metrics including vessel area density [58], vessel length fraction [58, 59], and vessel diameters [27] were extracted from the Hessian-filtered projection images (Table 1). These metrics were obtained from the projection images in the xy plane, because the de-shadowing process can potentially alter vessel morphology in the xz or yz planes [27]. Vessel area density is defined as the vessel area in the Hessian-derived mask divided by the total image area. Vessel length fraction was computed from a skeletonized image of the vessels and is defined as the total length of centerline pixels divided by the total image area. In some cases, these parameters may follow similar trends, but it is important to measure multiple endpoints to determine whether an increase in the vascular area is due to an increase in the number of vessels (total length), an increase in the size of existing vessels (diameter), or both [15]. The vessel diameter distribution indicates the relative contributions of small and large vessels to these metrics, and was extracted by determining the vessel width at each centerline pixel and computing a histogram.

2.3 Statistical analysis

All data are reported as mean ± standard error of the mean (SEM). A Wilcoxon Rank Sum test was performed to compare the two strains within each time point. The effect of time post-surgery on ischemic limb vessel area density and vessel length fraction within each animal was tested with a Kruskal-Wallis ANOVA followed by a post-hoc Tukey test for multiple comparisons. $P < 0.05$ was interpreted as significant.

#223146 - $15.00 USD Received 15 Sep 2014; revised 16 Oct 2014; accepted 29 Oct 2014; published 3 Nov 2014

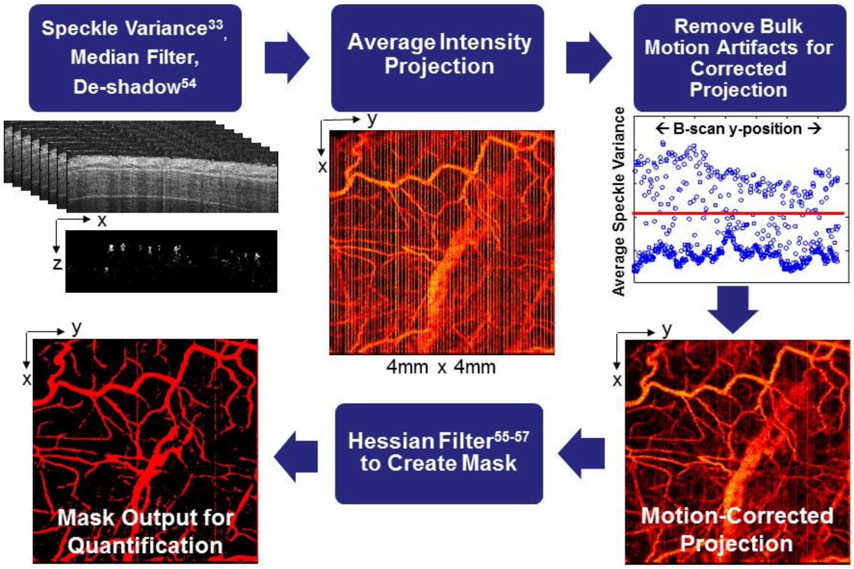

Fig. 2. Flow chart of image processing procedures for speckle variance images of the vasculature. Speckle variance [33] was computed over eight repeated B-scans collected at each spatial position in the volume, and the tissue was segmented using the corresponding structural image. The resulting speckle variance B-scans were then median filtered, de-shadowed [54], and projected in the depth dimension. B-scans with a high average speckle variance signal due to bulk motion artifacts were identified and replaced with the average of the nearest bulk motion-free B-scans, and a corrected average intensity projection was computed. The projected image was then Hessian filtered [55–57] to derive a vessel mask from which quantitative morphology metrics were extracted.

Table 1. Quantitative morphology metrics extracted from speckle variance OCT projection images

Morphology Metric	*Definition*
Vessel Area Density [58]	Vessel mask area / total image area
Vessel Length Fraction [58, 59]	Total vessel length / total image area
Vessel Diameter [27]	Diameter at each vessel centerline pixel, represented with a histogram to show distribution

3. Results

Speckle variance OCT of the ischemic limb adductor region enabled visualization of vessel remodeling over time in the Balb/c and FVB strains (Fig. 3). Quantification of vascular morphology metrics from average intensity projections of speckle variance volumes over ~1.5 mm in depth revealed significant differences in the vascular response to ischemia between the two strains. In the control (non-ischemic) limb, the vessel area density was significantly greater in Balb/c mice (Fig. 4(A)). At 3 days post-surgery, the vessel area density in the ischemic limb was equivalent for the two strains. At days 7, 14, and 19 (Balb/c) / 21 (FVB), the vessel area density in FVB mice was significantly greater than that in Balb/c mice ($p<0.05$). Vessel length fraction followed a similar trend, with a significant increase in this parameter for the FVB strain relative to Balb/c mice at days 7, 14, and 19/21 ($p<0.05$) (Fig. 4(B)). Furthermore, the temporal changes in these parameters were evaluated for each strain using a Kruskal-Wallis ANOVA and post-hoc Tukey test. In Balb/c mice, vessel area density and vessel length fraction in the ischemic limb did not increase significantly over time; rather, there was a significant decrease in both parameters between day 7 and day 19 ($p<0.05$). In contrast, vessel area density increased significantly from day 3 to day 7 and vessel length fraction increased significantly between days 3 and 14 in the FVB strain.

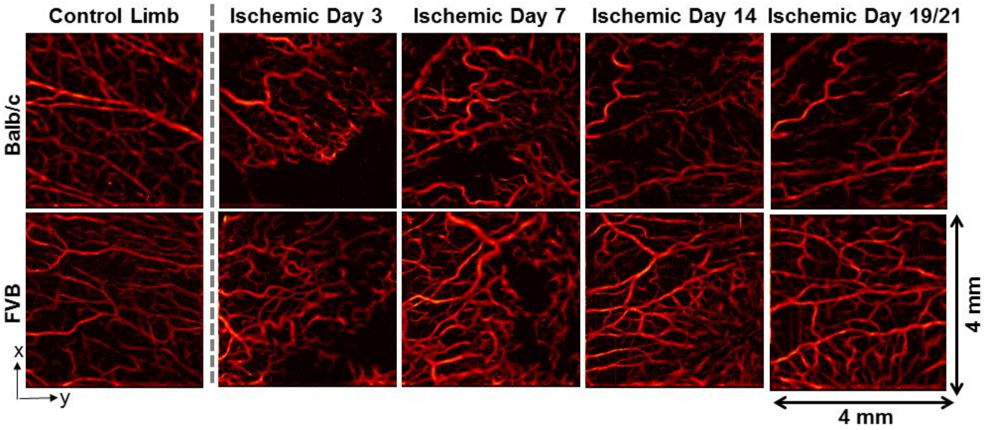

Fig. 3. Representative speckle variance OCT images of the adductor muscle from each mouse strain, including the contralateral control limb (far left) and the ischemic limb imaged non-invasively over a time-course. Images are shown for both Balb/c (top row) and FVB (bottom row) mice. The last imaging time point was day 19 for Balb/c mice and day 21 for FVB mice.

Strain-dependent differences were also observed in distribution of vessel diameters in the ischemic limb during recovery from HLI (Fig. 4(C)). At day 3, FVB mice had a greater length of vasculature with diameters less than 24 µm, while the distribution was similar between the two strains for larger vessel diameters at this time point. At day 7 post-surgery, the length of vessels with diameters from 36 to 124 µm was significantly greater in the FVB strain. Similar differences in the diameter distributions were observed at days 14 and 19/21 post-surgery in the 24-124 µm and 36-136 µm diameter ranges, respectively. In addition to the quantified differences in vessel morphology between the two strains in the proximal limb, differences in distal tissue fate were qualitatively observed that correlated with the OCT data. The ischemic paws of Balb/c mice had visible tissue necrosis, while the FVB strain did not suffer from this functional consequence of HLI. Lastly, structural OCT images from the adductor muscle region show changes in tissue structure beneath the skin that occur in the ischemic limb post-surgery, presumably due to inflammation (Fig. 5).

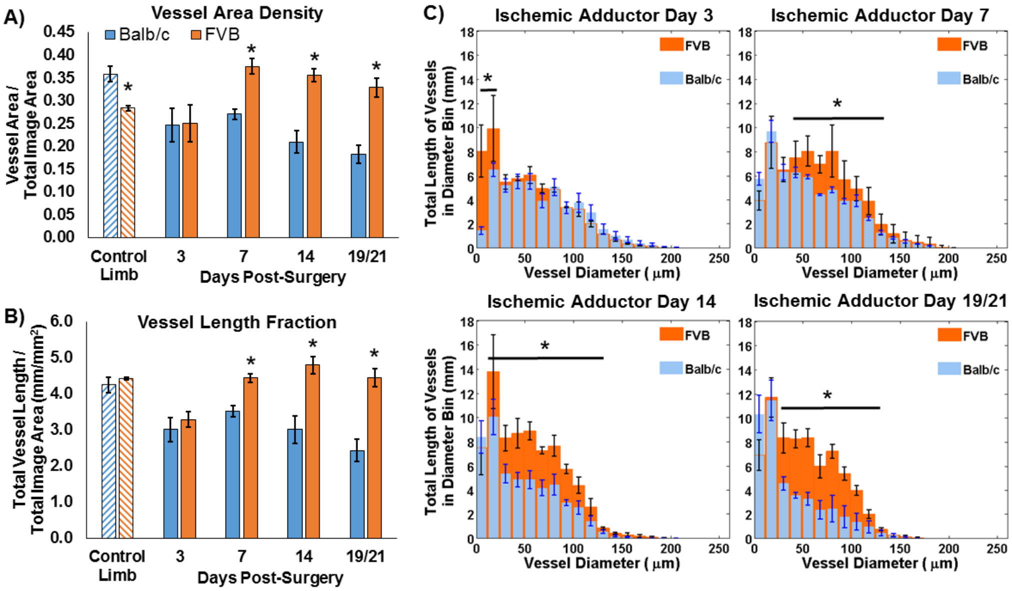

Fig. 4. Vascular morphology metrics were quantified from speckle variance OCT projection images for Balb/c (n = 4) and FVB (n = 3) mice. FVB mice showed increased (A) vessel area density and (B) vessel length fraction at day 7 and subsequent time points post-surgery in the ischemic adductor region relative to Balb/c mice (*p<0.05 between strains). Balb/c mice also showed a decrease in both parameters between days 7 and 19 (p<0.05), while vessel area density and length fraction increased for FVB mice between days 3 and 7 and days 3 and 14, respectively (p<0.05). (C) Significant differences in the length of vasculature within a given range of vessel diameters were also detected (*p<0.05 for indicated range of diameters). The last imaging time point was day 19 for Balb/c mice and day 21 for FVB mice.

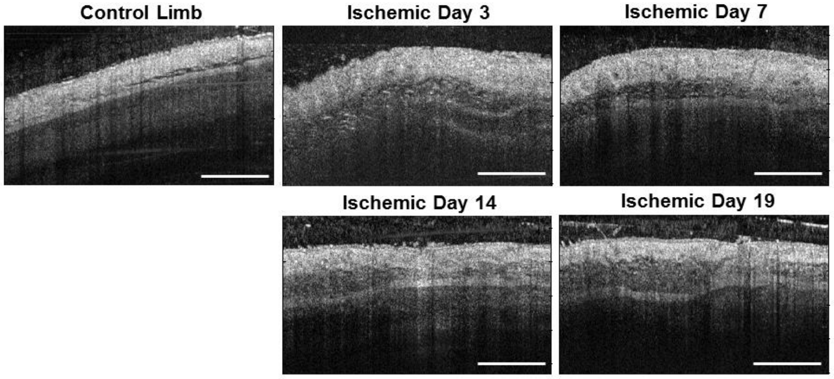

Fig. 5. Representative structural OCT images from the adductor muscle region, including the contralateral control limb (left) and the ischemic limb imaged non-invasively over a time-course. A change in tissue structure beneath the skin is observed in the ischemic limb, presumably due to inflammation. Scale bar is 1 mm.

4. Discussion and Conclusions

In this work, we have demonstrated the utility of speckle variance OCT [33, 43, 54] for quantitative, non-invasive monitoring of vascular remodeling in the mouse hind limb ischemia model of PAD. OCT fills a gap in the existing toolset for evaluating this model, with micron-scale resolution, imaging depth and field of view of several millimeters, and endogenous vessel contrast [27, 28]. The speckle variance method for imaging vessel morphology has several strengths, including sensitivity to flow in microvessels, angleindependence, fast acquisition, and little increase in computational complexity [54]. The application of speckle variance OCT for quantitative imaging of the vascular response to HLI has potential to provide new insight into the dynamics of vascular remodeling, as well as streamline the evaluation of novel therapies in preclinical trials.

To validate the OCT system, image preprocessing routines, and techniques for data analysis that are collectively necessary for investigation of vascular remodeling in the HLI model, it was necessary to first identify a reliable experimental model. The ability to differentiate the responses of two groups was validated through the comparison between a mouse strain with a robust response to ischemia (FVB) and a strain known to have poor recovery (Balb/c) [15, 16, 52, 53]. Variations in native collateral conductance and collateral remodeling have been observed among commonly used inbred strains, with Balb/c mice in particular exhibiting less collateral remodeling accompanied by severe ischemic tissue injury compared to other strains (e.g. A/J, C57BL/6) [52]. Additionally, tissue loss due to severe ischemia may reduce the speed and extent of collateral artery growth, since fluid shear stress and total flow are reduced [15]. In the current study, *in vivo* longitudinal quantification of vascular morphology in FVB mice reflected a greater vessel area density, length fraction, and diameter compared to Balb/c mice (Figs. 3 and 4). Balb/c mice demonstrated impaired recovery based on these metrics and also suffered from ischemic paw necrosis. Our results are similar to those in previous studies showing a lack of change in vessel density in the adductor of Balb/c mice using post-mortem histology [15], and a decreasing trend for Balb/c adductor perfusion at later time points using laser Doppler perfusion imaging [52]. Differences in trends between studies can be attributed to the severity of the surgical model, which ranges from a single ligation of the femoral artery [15] to multiple ligations and transection of a vessel segment as performed in the current work [17]. In contrast, FVB mice respond similarly to the A/J strain, with small native collaterals that undergo greater remodeling after femoral artery ligation (determined from laser Doppler perfusion imaging and post-mortem X-ray angiography and histology) [52].

The quantitative metrics for vessel density, length, and diameter quantified for this model are comparable and complementary to endpoints of vascular morphology collected with traditional post-mortem methods. At the terminal endpoint of a longitudinal vascular remodeling study, morphological parameters such as number of collateral vessels, vessel volume, vessel thickness and connectivity may be obtained from x-ray angiography [13, 15, 16] or micro-CT [17, 18], and high resolution capillary or arteriole density can be measured with histology by staining for CD31 or smooth muscle actin, respectively [9, 12–14]. Angiography and micro-CT provide a global view of the hind limb vasculature, while speckle variance OCT fills a gap in field of view between these global measurements and the two dimensional slices that are sampled with histology. Additionally, speckle variance OCT detects perfused vessels with contrast based on blood flow, while staining fixed tissues for histological examination will label all endothelial and/or smooth muscle cells regardless of whether the vessels were perfused *in vivo*. These data sets are complementary because they provide assessments of both functional vessel density (with OCT) and total vessel density (i.e. counting capillaries stained with CD31). In addition to providing important intravital measurements of vascular remodeling that are not captured with post-mortem analyses, non-invasive speckle variance OCT enables us to track these metrics in individual animals over time. Longitudinal assessment of individuals is particularly important for minimizing inter-animal variability, because even inbred strains of mice can have variability in pre-existing vasculature that impacts ischemic recovery [51]. Furthermore, in preclinical assessment of novel therapies, long term studies should be performed in order to capture the late-stage regression phase of the response that occurs in more relevant models of PAD such as diabetic mice, which is often omitted in studies where researchers must choose a few, terminal endpoints to analyze [60].

Although long term visualization of vasculature is valuable in itself as a qualitative endpoint, quantitative assessment of vascular remodeling enables a more robust evaluation of disease status or therapeutic efficacy [61]. Previous studies have applied quantitative analysis of OCT angiography data in several preclinical models, although to our knowledge, long term, non-invasive (through the skin) quantitative vascular metrics have not been previously demonstrated in ischemic skeletal muscle. Commonly used metrics for vascular morphology studies performed with OCT include vessel area density and vessel length fraction, which represent the area filled by vessels and the total length of vessels, respectively [58, 59, 61]. Vessel diameters have also been extracted [27], and the distribution provides insight into the contributions of vessels of various sizes to global measurements of length and density. Other parameters of interest include tortuosity and fractal dimension, which provide a measurement of vessel branching and architecture [27, 58, 61, 62]. Although longitudinal changes in blood flow have been quantified in the HLI model using Doppler OCT [26] and optical microangiography techniques [49], assessment of vessel morphology has been limited to qualitative observations [26, 49]. In this work, we applied quantitative morphology metrics that have been used in preclinical studies of tumors [27, 61], burn wounds [11], and healthy tissue [58] to non-invasively monitor the response to ischemia in skeletal muscle vasculature, and demonstrated their sensitivity for discriminating groups with different responses.

In comparison with OCT systems used in previous studies [26], the speed and penetration depth of the 100 kHz, 1060 nm swept-source system used here is well suited to imaging in the HLI model. While previous studies have utilized an 860 nm spectral domain system, the 1060 nm swept-source used here increases the theoretical depth limit for capturing flow in skeletal muscle vessels due to reduced scattering at longer wavelengths, and also reduces roll-off in imaging sensitivity with depth due to the improved spectral resolution at which the interference signal is sampled [63]. Previous studies have noted that arterioles lie in a deeper layer of the muscle (beginning >700 μm from surface) [49], and these vessels are critical to delivering oxygenated blood to peripheral tissues. For this reason, imaging deeper with OCT allows for a more thorough assessment of blood supply in the hind limb ischemia model that is not available using techniques with relatively shallow penetration such as microscopy. Additionally, swept-source lasers near 1300 nm will further improve imaging depths in the HLI model. Ideally, imaging should be performed over an area large enough to cover a region of interest such as the adductor, gastrocnemius, or distal femoral artery to comprehensively cover areas where vascular remodeling occurs. In previous studies [26], limitations to the OCT instrument necessitated acquisition of multiple C-scans to achieve this goal, and minimizing motion artifacts during long acquisition times was a significant challenge. The fast 100 kHz A-scan rate improves upon the 20 kHz imaging speed of the previous system used to image HLI, and thus volumes can be collected with reduced motion artifacts. Furthermore, larger areas can be scanned without increasing the acquisition time compared to the previous work.

Although the imaging speed was a significant improvement in this study, *in vivo* OCT is still susceptible to bulk motion artifacts due to respiration and heartbeat. Streaks due to motion artifacts (Fig. 2) may affect subsequent vessel segmentation procedures and quantification of morphology [64], so minimizing artifact signal while preserving vessel contrast in the image is desired. In this work, we developed an approach to minimizing these artifacts in the resulting vascular maps which consisted of identifying frames with bulk motion using an average B-scan variance threshold. After the motion artifact frames were replaced with the average of the nearest motion-free frames, the depth projections were largely free of high intensity bands corresponding to motion. Other post-processing techniques for reducing motion artifacts include frequency rejection filters [65] and segmentation of vessels in B-scans with a classifier algorithm [64]. The former is effective for periodic motion artifacts but may be less so for removal of bulk motion that is non-periodic [64, 65]. The latter can be applied to both periodic and non-periodic bulk motion, but the classifier algorithm requires a training set of manually segmented images [64]. There are also several methods available for addressing the challenge of motion artifacts in speckle variance OCT during acquisition, including the use of orthogonal scan patterns [34, 66], short acquisition times [62], optimizing frame rates (field of view) and gate length [43]. However, additional scans increase acquisition time and data storage/processing, and acquiring faster scans may compromise field of view and sensitivity to slow flow. We must cover a relatively large region of interest in the HLI model, so we developed a robust post-processing approach to minimize motion artifacts.

Similarly, several methods have been established for vessel segmentation and filtering in OCT angiography data sets. Approaches range from intensity thresholding and band pass filtering [62] to clutter rejection [67] and directional filters (Gabor) [34]. Here, we chose to implement a Hessian filter [55–57] due to speed of computation and the multi-scale estimation of vessel-like structures that is compatible with segmenting the range of vessel sizes observed in the HLI model. The Hessian filter extracts the principle directions of the image, detects vessels at any orientation, and is computed at multiple vessel scales [55]. In comparison, the Gabor filter requires a convolution at evenly spaced rotations to determine the orientation of maximum response, and the response must be computed at multiple scales [34]. This results in a greater computational burden compared to the Hessian filter approach. Compared to intensity-based methods, Hessian filters are less sensitive to noise and intensity variations, and are more selective in identifying vessel shape as the eigenvalues of the Hessian are used to locally detect vessels [55, 56]. Hessian filtering does not require prior manual removal of noise, and the resulting vessels are smoother in comparison to vessels segmented based on an intensity threshold [56]. Furthermore, the quantification of closeness (or likelihood) to a vessel structure for each pixel enables additional control in excluding noise from the segmented vessel mask.

In conclusion, understanding the mechanisms and dynamics of vascular remodeling processes is critical to the development of new pro- and anti-angiogenic therapies for treating pathological conditions from ischemia to cancer. Although models such as mouse HLI are widely used to assess the therapeutic potential of new treatments for PAD and other ischemia-related diseases, quantitative, high resolution methods for intravital, longitudinal measurements are lacking. To address this need, we developed speckle variance OCT methods for assessment of remodeling in the ischemic limb and demonstrated the sensitivity of our approach to detect strain-dependent recovery from ischemic injury. In this context, the quantitative morphology metrics (vessel area density, length fraction, and diameter) obtained from speckle variance OCT data were sensitive to differences in the vascular response to ischemia. Overall, this work confirms that speckle variance OCT is a promising technique for robust preclinical evaluation of novel therapies, an essential step for successful translation to early clinical trials.

Acknowledgments

The authors thank Megan Madonna and Constance Lents for assistance with experiments, and Andrew Fontanella for assistance with vascular image processing. This work was supported by a Vanderbilt Discovery Grant, NIH R21 HL109748, American Heart Association Grant-in-Aid 12GRNT 12060235, AHA Greater Southeast Affiliate Pre-doctoral Fellowship (D.R.M.), P.E.O. Scholar Award (K.M.P.) and NSF Graduate Research Fellowship DGE-0909667 (K.M.P.).